Supplementary Information for

Generation of time-varying OAM beams with space-time-coding digital metasurface

Jingxin Zhang,[a] Peixing Li,[b] Ray C. C. Cheung,[b] Alex M. H. Wong,[b,c,]* and Jensen Li[a,]*

[a] Department of Physics, The Hong Kong University of Science and Technology, Clear Water Bay, Kowloon, Hong Kong, China

[b] Department of Electrical Engineering, City University of Hong Kong, Hong Kong

[c] State Key Laboratory of Terahertz and Millimeter Waves, City University of Hong Kong, Hong Kong

* alex.mh.wong@cityu.edu.hk, jensenli@ust.hk

This PDF file includes:

Supplementary Text

Supplementary Figure S1 to S6

Supplementary Table S1 to S3

Supplementary Equation S1 to S4

1. Theoretical model for time-varying OAM beam

In this section, we give the details on modeling the time-varying OAM beam. Suppose coordinates for the measurement plane is (x, y, z) with fixed z and variable x and y. The metasurface is situated at $z = 0$ and we use another set of 2D coordinates (x', y') on the metasurface for clarity in this section. We also define the cylindrical coordinates on metasurface plane as (ρ', θ') and the cylindrical coordinates on the measurement plane as (ρ, θ).

To generate the time-varying OAM beam, we would like the reflection coefficient $r(\theta', t)$ of the metasurface to implement $\exp\left(-j\ell(t)(\theta' - \eta)\right)$ where $\ell(t) = Nt/T$

is the time dependent topological charge changing linearly in time and η is defined as the twisting angle (being a constant for the case without winding and time-dependent otherwise) of the time-varying OAM beam. However, we can only approximate such continuous version. As we know that the reflection coefficient has to be periodic in θ' to have a well-behaved OAM, we need to have integer $\ell(t)$ ranging from 0,1,2,… at time instants $t = 0, T/N, 2T/N$, etc. where N is a positive integer. Therefore, it is natural to implement the reflection phases changing in steps of T/N. $\ell(t)$ is then approximated by $\lfloor Nt/T \rfloor$ where $\lfloor \circ \rfloor$ is the floor function. On the other hand, our metasurface with the FPGA system implements a periodic modulation of period T. Such temporal periodicity requires us to discretize the θ'. The metasurface is then discretized into also N azimuthal sectors, with each sector spanning an angle of $2\pi/N$ and implementing the same response for the whole sector. $\theta' - \eta$ is then approximated by $\lfloor N(\theta' - \eta)/(2\pi) \rfloor 2\pi/N$. As a result, the argument of the reflection coefficient being implemented can be written as a function periodic in both θ' and t:

$$\arg\big(r(\theta', t)\big) = \alpha - \left\lfloor \frac{Nt}{T} \right\rfloor \left\lfloor \frac{N(\theta' - \eta)}{2\pi} \right\rfloor \frac{2\pi}{N}, \tag{S1}$$

to approximate $\arg\big(r(\theta', t)\big) \cong \alpha - \ell(t)(\theta' - \eta)$. We have added a constant phase $\alpha \cong \pi$ for the reflection part of the metallic ground plane of the metasurface while the second term of Eq. (S1) is the additional reflection phase introduced by the metamaterial atoms on the metasurface.

While later we will list the detailed coding scheme for each sector, for winding number $w = 0$, we can see that the sectors are always changing their reflection phases linearly (Fig. S1 and Table S2), so that it may be implemented in analog electronics by just different harmonic frequencies in changing reflection phase. On the other hand, for a non-zero winding number, e.g. $w = -1$ in main text, we set a time-dependent twisting angle by $\eta = 2\pi wt/T$. Then, the additional phase introduced into Eq. (S1) is defined as the twisting phase as

$$\varphi(t) = \ell(t)\eta(t) = 2\pi wN(t/T)^2, \tag{S2}$$

which is not linear in time and its implementation is enabled by using the combination

of digital electronics with the reconfigurable metasurface in this work.

With the reflection phase $r(\theta', t)$ realized by the metasurface, we can write down the field at the measurement plane $E(\rho, \theta, t)$ from the Fresnel diffraction formula:

$$
\begin{aligned}
&E(\rho, \theta, t) \\
&\cong e^{-j\frac{k}{2z}\rho^2} \iint E_{in}(\rho') r(\theta', t) e^{-j\frac{k}{2z}\rho'^2} e^{j\frac{k\rho\rho'}{z}\cos(\theta'-\theta)} \rho' d\theta' d\rho',
\end{aligned} \quad \text{(S3)}
$$

where k is the freespace propagation constant and $E_{in}(\rho')$ is the incident field from the horn (placed at a distance δ_h in front of the metasurface) approximated by $E_{in}(\rho') \cong \exp(-jk\sqrt{\delta_h^2 + \rho'^2})$. The integration is carried out over the aperture: the area of metasurface. We have assumed adiabatic limit that the modulation is much slower than the signal period. The harmonic time factor $\exp(j\omega t)$, the propagation phase $\exp(jkz)$ and a global amplitude (in E_{in}) are omitted for brevity. In main text, we define the field at the measurement plane as $E_b(\rho, \theta, t)$ for the case without the winding structure: setting constant. $\eta = \pi/8$ (the middle angle of the first sector spanning $2\pi/8$) substituted into $r(\theta', t)$ in Eq. (S3).

If we assume the discretization (in Eq. (S1)) is negligible and assume a circular aperture, Eq. (S3) can be further simplified (by substituting $r(\theta', t) \cong \exp\left(j\left(\alpha - \ell(t)(\theta' - \eta)\right)\right)$ with $\ell(t) = Nt/T$ as

$$
\begin{aligned}
&E(\rho, \theta, t) \\
&\cong e^{-j\frac{k}{2z}\rho^2} e^{j(\alpha - \ell(t)(\theta - \eta))} \int E_{in}(\rho') e^{-j\frac{k}{2z}\rho'^2} j^{\ell(t)} J_{\ell(t)}\left(\frac{k\rho\rho'}{z}\right) \rho' d\rho',
\end{aligned} \quad \text{(S4)}
$$

where J_ℓ is the Bessel function of order ℓ. Then, it becomes clear that the reflection phase $\alpha - \ell(t)(\theta' - \eta)$ translates into $\alpha - \ell(t)(\theta - \eta)$ for the phase structure of the time-varying OAM beam. We note that we are working in the adiabatic limit so that the phenomena is observable at the original signal frequency ω. On the other hand, we can also have the phenomenon of time-varying OAM beam at a higher harmonic at radial frequency $\omega + 2\pi m/T$. In this case, we only need to multiply an additional time-varying factor $\exp(j(\omega + 2\pi m/T))$ to the $r(\theta', t)$ being implemented.

2. Time-varying OAM beam with zero winding

To generate such a time-varying OAM beam, the space-time-coding scheme in one period of T can be pictured in Fig. S1(a), where each layer shows the phase distribution to generate different modes of OAM. For this illustration, we assume $w = 0$. The black stars represent the azimuthal locations for zero phase state. We find the zero phase for each mode of the time-varying OAM remains at the same azimuthal position, which is different from the $w = -1$ case described in Fig. 1 in the main text. The wavefront structure of the time-varying OAM beams with winding number $w = 0$ is shown in Fig. S1(b). If we join up the zero phase at different instants of time, the wavefront structure of zero phase (cyan color) looks like a wall, showing winding number $w = 0$ for the time-varying OAM beams.
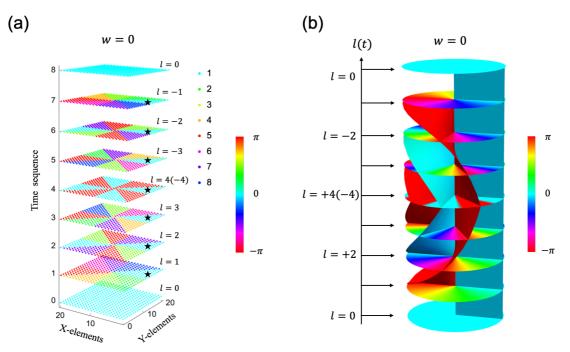

Fig. S1 Time-varying OAM beams with zero winding number w. (a) The space-time-coding scheme for time-varying OAM beams generation. (b) The wavefront structure of the time-varying OAM beams.

The simulated and measured field patterns of the time-varying OAM beam with $w = 0$ are shown in Fig. S2. The full-wave simulations are performed using the commercial software, CST Microwave Studio. We follow the space-time-coding scheme with 8 coding states in Fig. S1(a) and get the field pattern at different time instances of the reflected OAM beam as shown in Fig. S2(a) and (b). The measured

field patterns of the generated time-varying OAM beam are shown in Fig. S2(c) for comparison with the simulation results. The amplitude is not uniform for different phase coding states (see Fig. 2(c) and (e)) and we can observe the non-uniform intensity along the azimuthal direction in the simulated amplitude pattern especially for $l = 1$ and $l = 2$ cases. This error can be reduced by selecting the varactor diodes with lower series resistance and optimizing the unit structure of the metasurface to reduce the loss. The non-uniform amplitude has little influence on the phase pattern due to the high sensitivity of the phase measurement by the network analyzer. The field patterns of l and $-l$ show mirror symmetry according to the space-time-coding scheme in Fig. S1. This is different from the case of $w = -1$ described in the main text, where the field patterns show a twist in one period of T decided by winding number w as shown in Fig. 3(b).
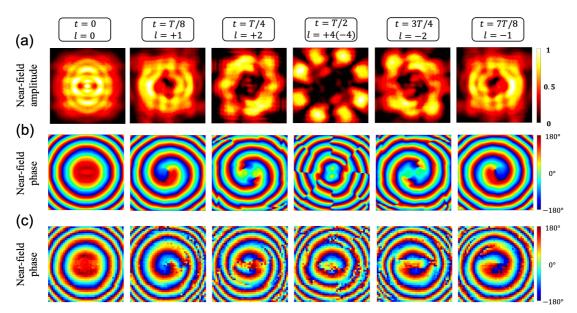

Fig. S2 Simulated and measured near-field patterns of the time-varying OAM beams with zero winding number w. (a) The simulated near-field amplitude patterns at different instances of time. (b) The simulated near-field phase patterns at different instances of time. (c) The measured near-field phase patterns at different instances of time.

3. Space-time-coding scheme

Fig. S3 illustrates the top layer of the designed metasurface with 20×20 elements and the bottom layer with a biasing network for space-time digital coding of

the metasurface. The pins on the side of the metasurface are used for the connection with the output pins of digital-analog conversion (DAC) module controlled by an FPGA system. At the bottom layer, these biasing lines can be designed to independently control the 8 azimuthal sectors θ_1 to θ_8 on the metasurface. By applying the corresponding bias voltages of the space-time-coding sequence on the 8 azimuthal sectors, the time-varying OAM beams can be generated. The biasing voltage network has more degree of freedom to control the elements for each row, but we only use the independent control of the 8 azimuthal sectors in this paper.
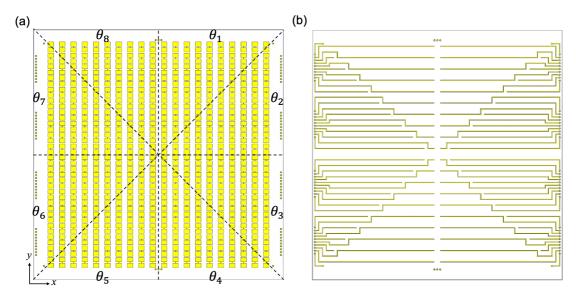

Fig. S3 The overall configuration of the space-time-coding digital metasurface. (a) The top layer of the designed metasurface with 20×20 elements. The metasurface is divided into 8 azimuthal sectors θ_1 to θ_8 for independent control. (b) The bottom layer of the metasurface with the biasing voltage network.

As shown in Table S1, we present the correspondence of the reflection phase, bias voltage, and coding digits. The listed reflection phase is the phase in addition to the π-phase reflection from the ground plane (as our convention). The corresponding coding digits are used in the following for brevity in representing specific reflection phases. The details for our space-time modulation scheme in Fig. 1(b) for the time-varying OAM beam generation with $w = -1$, and also the case of $w = 0$ (Fig. S1) are shown in Table S2, which are designed according to phase term $\exp(-j(Nt/T)(\theta -$

$2\pi wt/T)$ in Eq. (4). We remark that we only adopt eight different time frames (each frame is held for $T/8$) with eight coding states in a period of T to generate the integer $l(t)$, while the fractional OAM states are not considered for the implementation here.

Reflection phase	Bias voltages	Coding digits
0°	$3V$	1
45°	$7.5V$	2
90°	$8.1V$	3
135°	$8.4V$	4
180°	$8.6V$	5
225°	$8.9V$	6
270°	$9.4V$	7
315°	$11V$	8

Table S1 The correspondence of the reflection phase, bias voltage, and coding digits

Coding scheme for $w = 0$

Time	$l(t)$	θ_1	θ_2	θ_3	θ_4	θ_5	θ_6	θ_7	θ_8
$t = 0$	$l = 0$	1	1	1	1	1	1	1	1
$t = T/8$	$l = 1$	8	1	2	3	4	5	6	7
$t = T/4$	$l = 2$	7	1	3	5	7	1	3	5
$t = 3T/8$	$l = 3$	6	1	4	7	2	5	8	3
$t = T/2$	$l = 4(-4)$	5	1	5	1	5	1	5	1
$t = 5T/8$	$l = -3$	4	1	6	3	8	5	2	7
$t = 3T/4$	$l = -2$	3	1	7	5	3	1	7	5
$t = 7T/8$	$l = -1$	2	1	8	7	6	5	4	3
$t = T$	$l = 0$	1	1	1	1	1	1	1	1

Coding scheme for $w = -1$

Time	$l(t)$	θ_1	θ_2	θ_3	θ_4	θ_5	θ_6	θ_7	θ_8
$t = 0$	$l = 0$	1	1	1	1	1	1	1	1
$t = T/8$	$l = 1$	7	8	1	2	3	4	5	6
$t = T/4$	$l = 2$	3	5	7	1	3	5	7	1
$t = 3T/8$	$l = 3$	5	8	3	6	1	4	7	2
$t = T/2$	$l = 4(-4)$	5	1	5	1	5	1	5	1
$t = 5T/8$	$l = -3$	3	8	5	2	7	4	1	6

		θ_1	θ_2	θ_3	θ_4	θ_5	θ_6	θ_7	θ_8
$t = 3T/4$	$l = -2$	7	5	3	1	7	5	3	1
$t = 7T/8$	$l = -1$	1	8	7	6	5	4	3	2
$t = T$	$l = 0$	1	1	1	1	1	1	1	1

Table S2 The space-time-coding scheme for time-varying OAM generation with winding number $w = 0$ (upper panel) and $w = -1$ (lower panel). The coding digits 1 to 8 is corresponding to the coding states in the Table S1. The $l(t)$ denotes the time-varying topological charge at different time frames with a duration of $T/8$. The θ_1 to θ_8 represent the 8 azimuthal sectors of the metasurface.

According to the space-time-coding scheme in Table S2, we average the power reflected from the eight azimuthal sectors of the metasurface for different time frames with corresponding coding states distribution. The averaged power efficiencies for different OAM mode generation are listed in the Table S3 below. These power efficiencies are all above 80%.

Time	OAM mode	Power efficiency
$t = 0$	$l = 0$	97.56%
$t = T/8$	$l = 1$	81.87%
$t = T/4$	$l = 2$	82.25%
$t = 3T/8$	$l = 3$	81.87%
$t = T/2$	$l = 4(-4)$	84.26%
$t = 5T/8$	$l = -3$	81.87%
$t = 3T/4$	$l = -2$	82.25%
$t = 7T/8$	$l = -1$	81.87%

Table S3 The power efficiency of the generated time-varying OAM at different time frames with different OAM modes.

For the modulation frequency, it is possible to obtain a much shorter modulation period than 1ms (the modulation period in our work), depending on the electronics, currently limited by the analog electronic chips being used. Generating 8 channels of different DC biases with 16-bit resolution analog voltage levels requires multiple clock cycles; the fact that our DAC (digital to analog converter) chips operate in a serial fashion further slows the modulation speed. On the other hand, the use of varactors and high-precision DAC enable us to tune/adjust voltage levels of every channel flexibly whenever needed. The modulation speed can be increased by using DACs which feature

a parallel data transfer capability and faster stabilization time. One can also redesign the metasurface unit cells to use, as opposed to varactors, several pin diodes, which can be excited with digital bias signals. An example of a 4-level reflection phase reconfigurable metasurface with MHz modulation speed is reported in [Adv. Mater. 31, 1904069 (2019)]. Nonetheless, the current modulation speed in this paper is sufficient to elucidate the key physical effects as one would observe for modulation at the MHz time level.

4. Dynamic near-field pattern measurement of the time-varying OAM beams by using two probes.

In microwave experiments, the planar near-field scanning system is widely used for near-field pattern measurement or far-field radiation pattern calculation. However, for measuring a time-varying field pattern, as the measured S-parameters in time domain can start at any instant within one modulation cycle, the fields probed at different positions cannot be compared with each other directly. Here we use two probes as shown in Fig. S4. One probe S is moveable for the near-field scanning to measure the S-parameters for each pixel. The other reference probe R is fixed at Point 0 (P0) close to but outside the scanning range used to receive a reference signal for synchronization processing. The space-time-coding digital metasurface generates the time-varying OAM beams upon illumination by a feed horn. The feed horn, probe R, and probe S are connected to Ports 1, 2, and 3 of a vector network analyzer (VNA), respectively. The VNA works in the continuous wave (CW) stimulus mode to measure time-domain S-parameters within the sweep time covering several periods of the time-varying OAM beams. At time t, we start the first measurement and obtain the synchronized time-domain phase of S21(t) from probe R measured at P0, and S31(t) from probe S measured at P1 as shown in Fig. S5(a), where the sawtooth phase waveforms are simplified examples to illustrate the measurement process. At time $t + \Delta t$, the probe S is moved from P1 to P2, and the probe R keeps the fixed position at P0. The measured phase waveform S21($t + \Delta t$) has a time delay Δt compared with S21(t) as can be seen in Fig. S5(b). And the phase waveform S31($t + \Delta t$)) at P2 is not synchronized

with S31(t) at P1. As S21 is measuring the same point, only subject to a time shift. Δt can be extracted (either in time domain or by Fourier transform). Then we can use the calculated Δt to modify the waveform for synchronization as shown in Fig. S5(c). The S31(t) at P2 is synchronized with S31(t) at P1 after the above synchronization processing. Similarly, we can synchronize S31(t) for every pixel in the scanning range to obtain the dynamic near-field amplitude and phase pattern of the generated time-varying OAM beams.
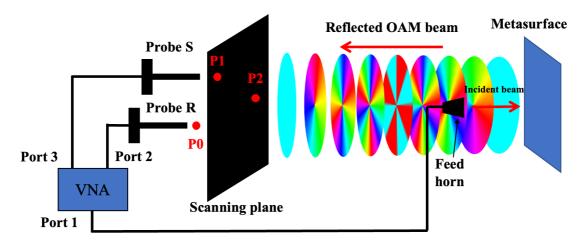

Fig. S4 The schematic of dynamic near-field pattern measurement for the time-varying OAM beams by using two probes.
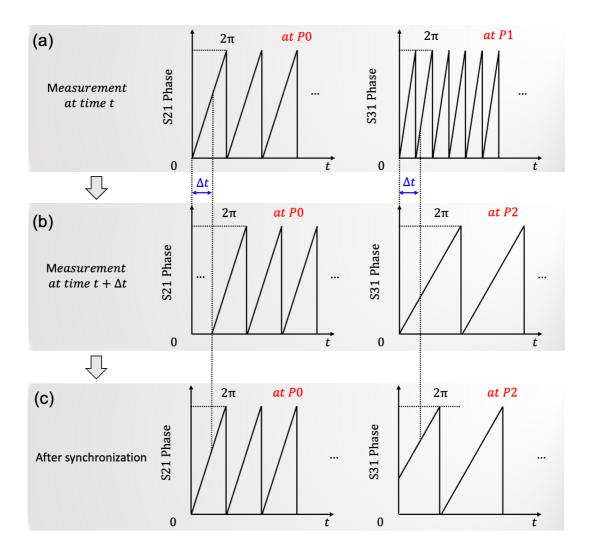
Fig. S5 The illustration of the synchronizing process for dynamic near-field pattern measurement of the time-varying OAM beams

To illustrate the synchronization effect, at the time instant of $t = 0$ and $t = T/8$, the phase of S31(t) before synchronization and after synchronization for all pixels are shown in Fig. S6. The T denotes the period of the time-varying OAM beams elaborated in the manuscript. As can be seen, Fig. S6(a) shows the measured time-domain S31(t) with t=0, corresponding to the OAM mode $l = 0$. However, the time of each measurement by the probe S during the scanning process can be any moment in the modulation cycle. Then the measured reflection phase in each pixel tends to be random. After the synchronization, the phase pattern in Fig. S6(b) shows the spherical wave with OAM mode $l = 0$. Similarly, Fig. S6(c) and Fig. S6(d) show the phase patterns before

and after synchronization at $t = T/8$ for OAM mode $l = 1$. We note that we have associated a probe R for the synchronization purpose. The S11 signal at the horn can be another possible candidate to serve as probe R in performing synchronization as well.
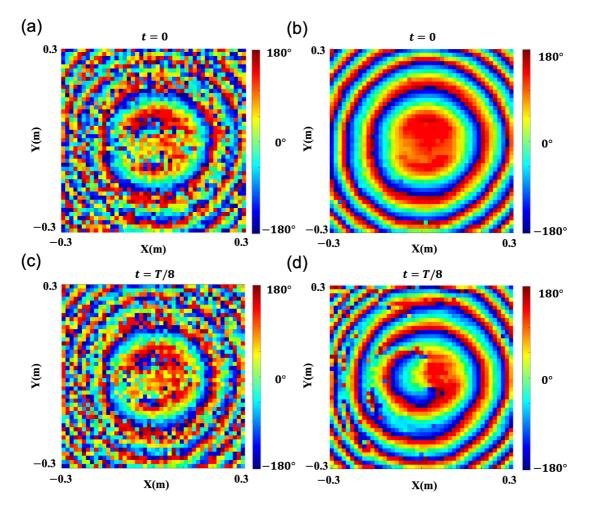

Fig. S6 The measured reflection phase S31(t) from probe S before synchronization and after synchronization for all pixels. (a) The reflection phase of S31(t) at $t = 0$ before synchronization. (b) The synchronized reflection phase of S31(t) at $t = 0$. (c) The reflection phase of S31(t) at $t = T/8$ before synchronization. (d) The synchronized reflection phase of S31(t) at $t = T/8$.